International Journal of Physical Modelling in Geotechnics
Volume 14 Issue 2

Use of null gauges to monitor soil stresses during excavation in a centrifuge
Li, Talesnick and Bolton

International Journal of Physical Modelling in Geotechnics, 2014, **14**(2), 40–53
http://dx.doi.org/10.1680/ijpmg.13.00021
Paper 1300021
Received 26//2013 Accepted 06/03/2014
Keywords: granular materials/models (physical)/retaining walls

ice
Institution of Civil Engineers
publishing

Use of null gauges to monitor soil stresses during excavation in a centrifuge

[1] **Yuchen Li** BEng, PhD
Geomechanics Engineer, Schlumberger, Beijing, China

[2] **Mark Talesnick** BSc, MSc, DSc
Associate Professor, Department of Civil and Environmental Engineering, Technion-Israel Institute of Technology, Haifa, Israel

[3] **Malcolm Bolton** MA, MSc, PhD
Professor, Geotechnical and Environmental Group, University of Cambridge, Cambridge, UK

A centrifuge test is presented that tracks the earth pressures around a stiff retaining wall, propped at the top, during in-flight excavation in dry sand. The test featured the first use in a centrifuge of a new earth pressure cell, the null gauge, which is designed to avoid measurement errors due to soil arching around flexible cells. Any tendency for membrane deflection is detected and quickly countered by applying a measured air pressure inside the cell. A sequence of centrifugal loading, unloading and reloading was conducted prior to any excavation. Null gauge measurements of (analogue) vertical stress showed some hysteresis from which the effects of boundary friction were assessed. Small corrections could be made using silo theory. Measurements of initial horizontal earth pressures conformed to conventional empirical estimates. The process of in-flight excavation using a scraper was monitored, and found to generate lateral pressure spikes owing to scraper penetration. These were analysed and found to fit an estimate based on soil compaction effects. Finally, the horizontal pressures during excavation are presented. Mobilised passive pressures are found to be non-linear with depth beneath the excavation, confirming the importance of excavating soil in flight rather than simulating the process using a heavy fluid.

Notation

B	width of the scraper
b	width of the strong box
f	friction force on soil–strong box interface
H	wall height
K	horizontal earth pressure ratio
K_a	fully active earth pressure ratio
K_p	fully passive earth pressure ratio
K_0	lateral earth pressure ratio at rest
$K_{0,\ \mathrm{OCR}}$	lateral earth pressure ratio at rest in over-consolidation
N	gravity level
N_q	bearing capacity factor for surcharge
N_γ	bearing capacity factor for self-weight
p'	mean effective stress
y_0	depth of the diaphragm of the earth pressure cell
z	depth of soil
γ_{soil}	unit weight of sand (dry)
$\delta_{\max}$	maximum horizontal wall movement
μ	average friction ratio between sand and strong box inner face
σ_{ult}	soil stress under a shallow foundation at bearing failure
σ_h'	horizontal earth pressure
$\Delta\sigma_h'$	horizontal stress increase due to scraper penetration
σ_v'	vertical earth pressure
$\Delta\sigma_v'$	vertical stress increase due to scraper penetration

ϕ'	sand friction angle
ϕ'_{crit}	critical state angle
ϕ'_{max}	peak shear angle

1. Introduction

The aim of centrifuge modelling is to recreate full-scale stresses in a convenient small-scale model prior to the instigation of some process of interest. Insufficient attention has been paid in the past to the use of earth pressure measurements to validate the common assumptions regarding initial soil conditions in such models, and the response during the construction process. The aim of this paper is to demonstrate the first use in a geotechnical centrifuge of the null-displacement earth pressure gauge developed by Talesnick (2005). It will be shown that common assumptions regarding K_0 and side friction can be refined in the light of actual measurements. Of more significance, the unexpected influence of stresses induced by an in-flight actuator can be observed.

2. Set-up of the centrifuge model

A centrifuge plane strain model was tested at 60***g*** to simulate half of a top-propped excavation in sand. Dry loose Hostun sand with a relative density of 47% was prepared in a rectangular test box using the Cambridge sand pourer (Madabhushi *et al.*, 2006). The properties of the Hostun sand are summarised in Table 1.

The test was designed to model a propped excavation retained by a very stiff wall. A schematic view of the test set-up is shown in Figure 1(a). A two-axis servo actuator was installed on top of the test box to provide in-flight controlled excavation. The detailed performance and specifications of the actuator are given by Haigh *et al.* (2010). A T-shaped blade was attached to the sliding housing of the actuator to perform in-flight sand scraping. The model wall was made of 9·6 mm thick aluminium alloy plate, which was equivalent in flexural stiffness to an 850 mm thick concrete wall at prototype scale. It was initially embedded 125 mm deep prior to the test. Two aluminium rods were used to model pre-stressed props on the retaining wall. The props supported the wall 40 mm above the retained soil surface, to allow the scraper to work beneath them. The initial propping force was 70 N prior to excavation, and the compression stiffness of the props was measured as 900 N/mm. A low-level bin was provided remote from the wall on the side to be excavated, with a feeder slope, so that sand could be scraped away layer by layer from the excavated side of the wall. The slope was sited sufficiently far away from the wall not to significantly modify initial conditions.

Sand properties parameters	Value
Minimum void ratio, e_{min}	0·555[a]
Maximum void ratio, e_{max}	1·067[a]
Specific solid density	2·65
Critical state friction angle, ϕ'_{crit}: °	33
D_{50}: mm	0·45
Uniformity coefficient, U_c	1·637

[a]Value according to Stringer (2012)

Table 1. Properties of Hostun sand

Two digital cameras (Canon Powershot G10, 14·7 megapixels) were installed to take photographs on both sides of the wall through a poly(methyl methacrylate) (PMMA) window. Soil movements beside the wall during the excavation were calculated using particle image velocimetry (PIV). The detail of the technique was introduced by White *et al.* (2003).

Six earth pressure cells were installed in the centrifuge model to measure earth pressures at different positions, as shown in Figure 1(b). Three pressure cells were used to measure horizontal earth pressures, and three cells were used to measure vertical earth pressures. One pressure cell was put on the soil surface on the retained side for reference. The codes, sizes and positions of the pressure cells are summarised in Table 2.

2.1 New pressure cell with null deflection

Traditional pressure cells rarely measure soil pressure accurately, as their flexible sensing diaphragm alters the soil stress distribution. A recent review of the use of earth pressure cells (Dave and Dasaka, 2011) concluded that traditional cells require calibration under conditions identical to their use if reliable data are to be acquired. Take and Valsangkar (2001) used exhaustive calibration procedures to obtain acceptable data of earth pressures in centrifuge models.

A new type of earth pressure cell developed by Talesnick (2005) has been used in the centrifuge model test reported here. Any tendency for the cell diaphragm to deflect is immediately sensed by strain gauges and countered by applying a controlled air pressure inside the sealed cell so that the deflection of the diaphragm remains negligible. The air pressure is continuously monitored and has been termed the ‘null’ pressure. A typical pressure cell is shown in Figure 2(a); the servo-control procedure, operating through a LabVIEW (National Instruments) program, is given in Figure 2(b). Deflection of the diaphragm is kept within tight bounds so that the cell is almost perfectly stiff under working conditions, eliminating the possibility of under-registration as a response to soil arching.

This sensing technology has been confirmed in small-scale laboratory tests at 1***g*** (Talesnick *et al.*, 2008, 2011), but this is the first trial in a centrifuge model test. The accuracy of the earth pressure cell depends on the accuracy and resolution of

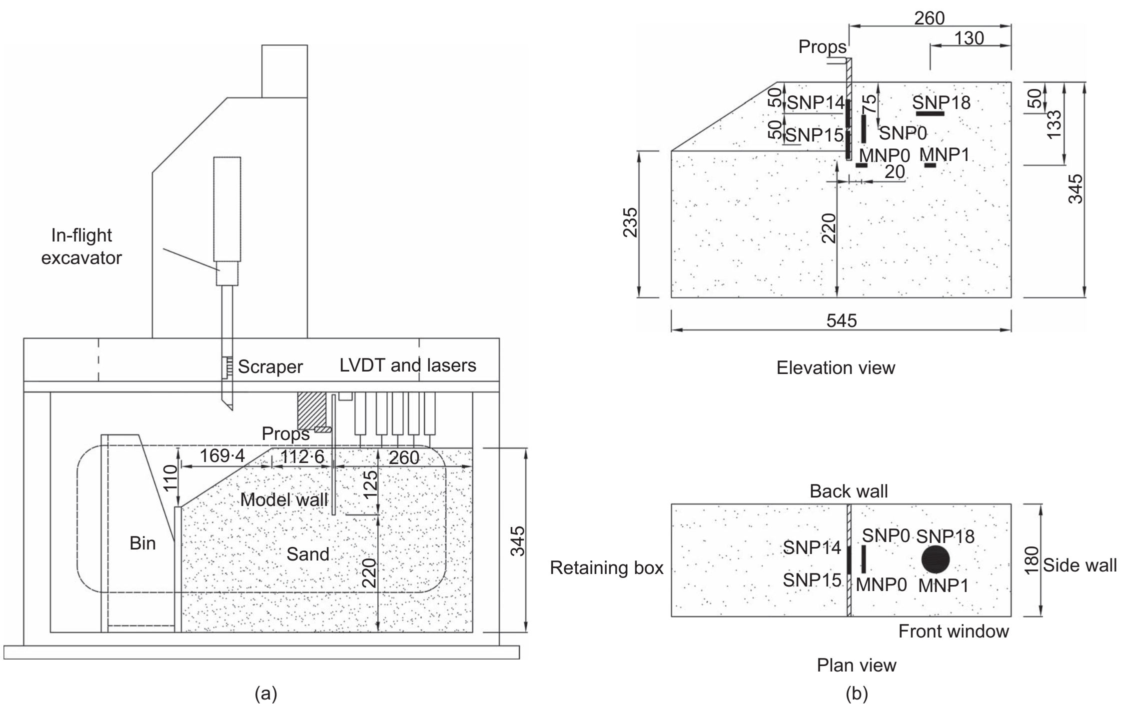

Figure 1. Overall experimental package and earth pressure cell positions: (a) schematic view of centrifuge model; (b) the positions of the earth pressure cells

the air pressure balancing system. In the centrifuge test, diaphragm deflection was maintained within $\pm 0{\cdot}1$ μm, which is equivalent to $\pm 0{\cdot}4$ kPa of net pressure on the diaphragm.

In the centrifuge testing set-up the null gauges were deployed in two modes: (*a*) as contact (flush mounted) pressure sensors on the excavation side of the wall and (*b*) as embedded (in mass) soil pressures sensors on the active side of the wall.

When deployed as a vertically mounted contact pressure sensor (SNP14 and SNP15) the registered null pressure is taken to be a true measure of the average applied lateral earth pressure, at the centre of the cell. This can only be explored in centrifuge tests, where there is a pressure gradient across the face. Strict verification was not possible in these tests owing to the relatively large diameter (23 mm) of the null cells compared to the depth of sand against the retaining wall used in this trial

Code	Diameter of sensing diaphragm:mm	Burial depth:mm	Stress orientation	Note
SNP0	23	75	Horizontal	Retained side, close to wall
SNP14	23	50	Horizontal	Excavated side, on wall
SNP15	23	100	Horizontal	Excavated side, on wall
SNP18	23	50	Vertical	Retained side, far from wall
MNP0	23	133	Vertical	Retained side, close to wall
MNP1	23	133	Vertical	Retained side, far from wall
SNP7	23	0	Vertical	Reference pressure cell

SNP0, SNP14, SNP15 and SNP18 were 6 mm thick, MNP0 and MNP1 were 5 mm thick.

Table 2. Summary of pressure cell locations and orientations

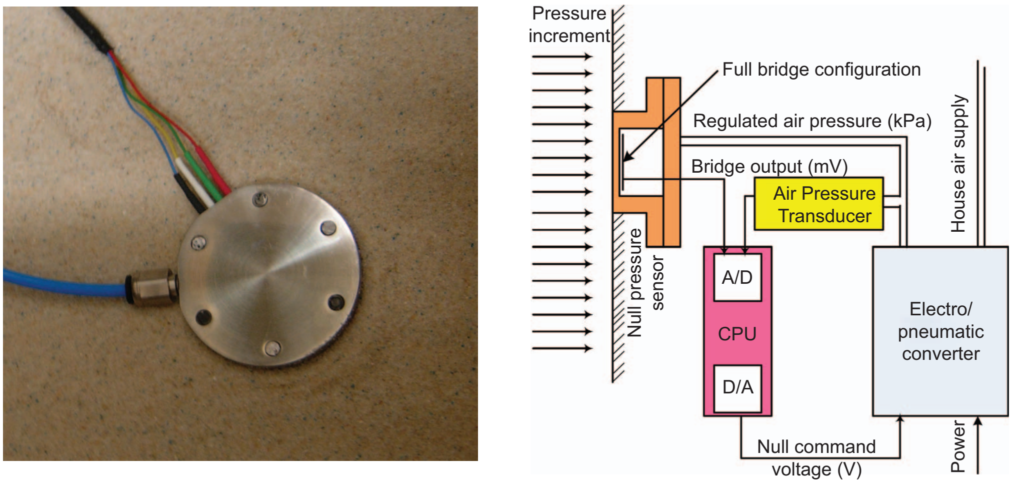

(a) (b)

Figure 2. New pressure cell: (a) Example of the pressure cell; (b) null loop algorithm, after Talesnick *et al.* (2014)

(125 mm). A new generation of 6 mm diameter gauges is currently in use on the Cambridge centrifuge.

In the case of embedded deployment two corrections may need to be applied to the registered null pressures. For pressure sensors embedded horizontally (SNP18, MNP0, MNP1), additional pressure is generated as the system strives to null the reading owing to the increased self-weight of the membrane in the increased acceleration field. This effect introduces a systematic error and was corrected by deducting from each gauge the reading from the reference pressure cell which was deployed on the sand surface (SNP7). A second correction must be applied to the null pressure registered by the embedded pressure cells due to their incompressibility relative to the surrounding sand: the measured null pressure is always larger than the soil pressure in the absence of the pressure cell. Therefore an over registration ratio (ORR) should be applied to deduce the 'true' earth pressure. According to Talesnick (2013), for an embedded pressure cell with a specific aspect ratio (thickness/diameter) the ORR coefficient is independent of grain size, density, soil stiffness and loading history. Here an ORR of 1·04 was used to correct pressure cell readings according to the calibration results of Talesnick (2013). Therefore the corrected earth pressure is represented by

$$1. \quad \sigma' = \left(p'_{\mathrm{reg}} - p'_{\mathrm{r}}\right) \Big/ \mathrm{ORR}$$

where p'_{reg} is the registered null pressure and p'_{r} is pressure registered at the reference cell.

Earth pressure sensors which are intended to 'float' in the sand model were installed when sand had been poured to the required level as in Figure 1. Figure 3 shows pictures taken when earth pressure cells were installed. Pressure cells measuring vertical soil pressure were placed directly on the sand surface, so that poured sand would automatically fix their positions. Cells measuring horizontal earth pressure were placed after sand had been poured to their intended mid-level. The cell was then carefully embedded until half of it was submerged in sand, its orientation being confirmed by checking parallelism with the neighbouring model retaining wall; sand pouring could then continue. Cells mounted in the model wall were installed in pre-drilled depressions with their sensing faces flush with the wall surface prior to sand-pouring. Further installation details can be found in Li (2013).

Each soil pressure cell requires a complete feedback loop to maintain the sensing diaphragm in the undeflected state. In the centrifuge test, each pressure cell therefore needs support from the following equipment

- a servo-controlled electro-pneumatic converter, which regulates the null pressure according to a signal output from the central processing unit (BB1-Proportion Air, 0–10 Vdc, 0–700 kPa))
- a strain-gauge-based air pressure transducer used the measure the null pressure (Honeywell-Sensotec JTE100)
- two analogue input channels (NI-SCXI 1000 chassis, NI-SCXI 1600 module, NI-SCXI 1520 module), which receives the signal of the soil pressure sensor and the null pressure transducer
- a single analogue output channel used to transmit a voltage command to the electro-pneumatic converter (NI-SCXI 1124 module).

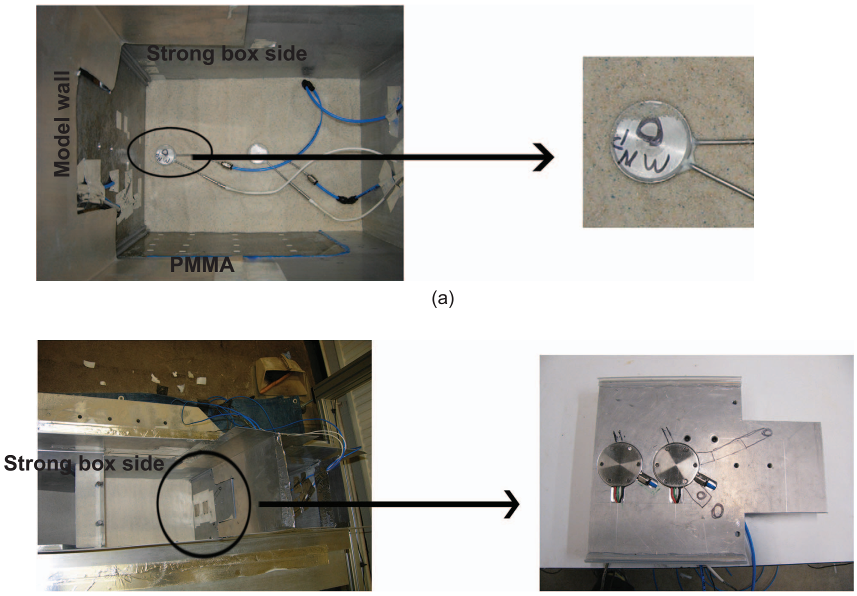

Figure 3. Earth pressure cell installation

3. Earth pressures during centrifuge acceleration and deceleration

During the spin-up stage, soil stress at a certain depth in the test package changes with centrifuge rotation speed. When the ***g***-level increases, soil settles due to increased vertical stress, whereas the aluminium strong box is relatively rigid. The difference in settlement between the sand and the strong box causes upward friction on the sand as ***g***-level increases. This friction is recognised in principle by centrifuge experimentalists, but contributory measurements are scarce: the issue is discussed in the context of model reinforced soil walls by Santamarina and Goodings (1989). A special spin-up program was designed to study the effects of side wall friction in centrifuge tests. The test schedule is shown in Table 3. The overall spin-up sequence was divided into a loading stage, an unloading stage and a reloading (second loading) stage. The test package was accelerated to 40***g*** in increments of 10***g***, then unloaded to 1***g*** in the unloading stage, followed by a second spin up to 60***g*** in the reloading stage. Enough time was left until all earth pressure cell readings had stabilised before they were taken. In theory, in the loading and reloading stages, friction forces on the sand should be upwards due to sand settlement. In the unloading stage, friction forces should be downwards due to the rebound of the sand.

3.1 Vertical earth pressures: data and model

A typical plot of earth pressure measurement against average acceleration level of the test package is shown in Figure 4(a). The earth pressure measurement comes from SNP18, which measured vertical stress at a relatively shallow depth. Acceleration data were obtained from the accelerometer measurements modified according to the radial distance of SNP18. From the figure, an average fluctuation of about 5 kPa in earth pressure reading is observed. This fluctuation reflected the process of the electro-magnetic valve letting air through to balance soil pressure which changed when the gravity level of the test package changed. When the rotation speed of the beam centrifuge was stabilised in a certain stage (e.g. 30***g***), a dense data zone can be observed. The average earth pressure in the dense zone was taken for analysis afterwards. Average pressures were picked to represent the earth pressure in

Gravity level: ***g***	1	10	20	30	40	50	60
Loading							
Unloading							
Reloading							

Table 3. Testing procedure in spin up stage

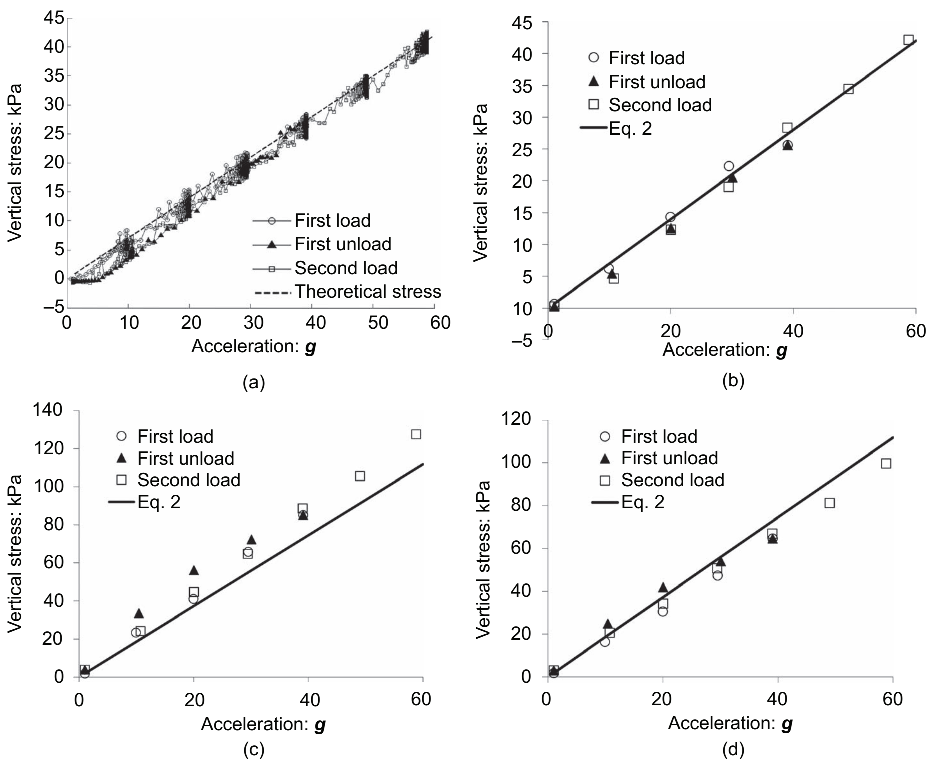

Figure 4. Vertical earth pressure measurements in spin-up stage: (a) vertical stress measurements from SNP18; (b) simplified SNP18 measurements; (c) MNP0, close to the wall; (d) MNP1, far from the wall

each dense data zone, and plotted in Figure 4(b). This method is also used in other earth pressure plots.

In theory, if side friction is neglected, vertical pressure in the soil can be expressed as

$$2. \quad \sigma_{\mathrm{v}}' = N\gamma_{\mathrm{soil}}z$$

where N is gravity level, γ_{soil} is the unit weight of dry sand and z is the depth of the sensing diaphragm below the soil surface. Theoretical earth pressure is in a linear relationship with virtual gravity level, as drawn in Figure 4(a). It is shown in the figure that the measured earth pressures fit the theoretical line fairly well during all loading–unloading–reloading stages. The correspondence also confirmed that earth pressure cell measurements were not affected by soil stress history, which is rarely achieved in earth pressure measuring practice (e.g. Clayton and Bica, 1993). The reliability of the new earth pressure cell measurements is considered sufficient for further analysis.

Figures 4(c) and 4(d) show the vertical earth pressures measured at MNP0 and MNP1, which were buried deeper than SNP18. MNP0 was installed close to the retaining wall toe, and MNP1 was far from the wall toe. In both plots, vertical pressures measured in the unloading stage were significantly higher than those in the loading and reloading stages at the same gravity level, which confirms the existence of boundary friction effects. This difference is not obvious in Figure 4(b) for SNP18 which was embedded at a shallower depth, where the influence of side friction was correspondingly smaller. Generally, the vertical pressure in the loading stage was very similar to what was measured in the reloading stage, suggesting that side friction is not affected by stress history.

Vertical earth pressure at MNP0 (Figure 4(c)) was above the theoretical line, and the pressure at MNP1 (Figure 4(d)) was mostly below the theoretical line. For MNP1, which was far from the model wall, friction between the sand and the strong box was probably the main cause of a lower-than-theory vertical pressure in the loading/reloading stage and higher-than-theory vertical pressure in the unloading stage. For MNP0, in addition to the friction between the sand and strong box, the soil pressure was also influenced by the model wall. The wall settled more than the sand due to its larger unit weight, which resulted in a downward friction on the surrounding sand in the loading and reloading stages. Vertical pressure underneath the wall toe was also increased due to the existence of the heavy wall. Accordingly, the earth pressures registered by MNP0 were higher than the theoretical free-field values.

The hysteresis in measured vertical stress on centrifugal loading–unloading–reloading, that is evident in Figure 4, can presumably be attributed to friction between sand grains and the strong box inner surface (milled aluminium surface and smooth PMMA surface). A simple model for estimating the friction in the centrifuge test is proposed here. Several simplifications are made.

- Vertical pressure is uniformly distributed at any given depth, and down drag of the model wall is ignored. This is valid for soil far from the model wall.
- Friction is only generated by horizontal pressure on the back wall and the front window: $f=2\mu\sigma_{\mathrm{h}}'$, where μ is the average friction ratio between sand and the strong box. It is assumed that the magnitude of relative movement does not affect the friction force.

A thin horizontal layer across the strong box, with unit depth into the paper, is considered for equilibrium analysis. Under the assumptions above, a free body diagram of the thin layer in the loading and unloading stages can be drawn as shown in Figure 5.

In the loading phase, the friction force on the sand is upwards due to sand settlement. Vertical force equilibrium at vertical direction in the layer can be written as

3. $$\gamma_{\mathrm{soil}}b\,dy+\sigma_{\mathrm{v}}'b=2\mu\sigma_{\mathrm{h}}'dy+\left(\sigma_{\mathrm{v}}'+d\sigma_{\mathrm{v}}'\right)b$$

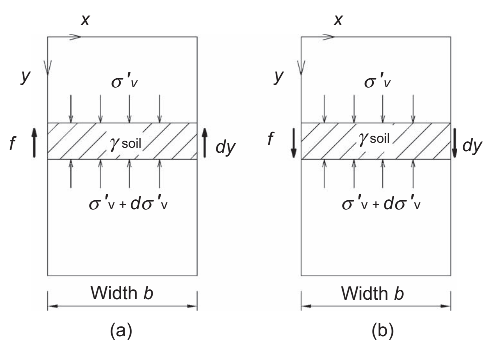

Figure 5. Free body diagrams of a thin sand layer: (a) loading phase; (b) unloading phase

Horizontal earth pressure will be taken as

4. $$\sigma_{\mathrm{h}}'=K_0\sigma_{\mathrm{v}}'=\left(1-\sin\phi_{\mathrm{crit}}'\right)\sigma_{\mathrm{v}}'$$

Vertical soil pressure at a depth of y_0 can then be solved from Equations 3 and 4

5. $$\sigma_{\mathrm{v}}'=\frac{b\gamma_{\mathrm{soil}}}{2\mu K_0}\left[1-e^{-2\pi K_0(y_{\mathrm{o}}/b)}\right]$$

Similarly, in the unloading phase, vertical soil pressure at depth of y_0 can be expressed as

6. $$\sigma_{\mathrm{v}}'=\frac{b\gamma_{\mathrm{soil}}}{2\mu K_0}\left[e^{2\mu K_0(y_{\mathrm{o}}/b)}-1\right]$$

Therefore the measured vertical stresses in loading and unloading can be used to estimate the average friction ratio μ when the box width b, K_0 and y_0 are known. With vertical stress measurements in the loading and unloading stages from SNP18 and MNP1, embedded at different depths, μ can be varied to fit the measurement data for the least average error. It is found that μ=0·27 gives the best fit to the data. Figure 6

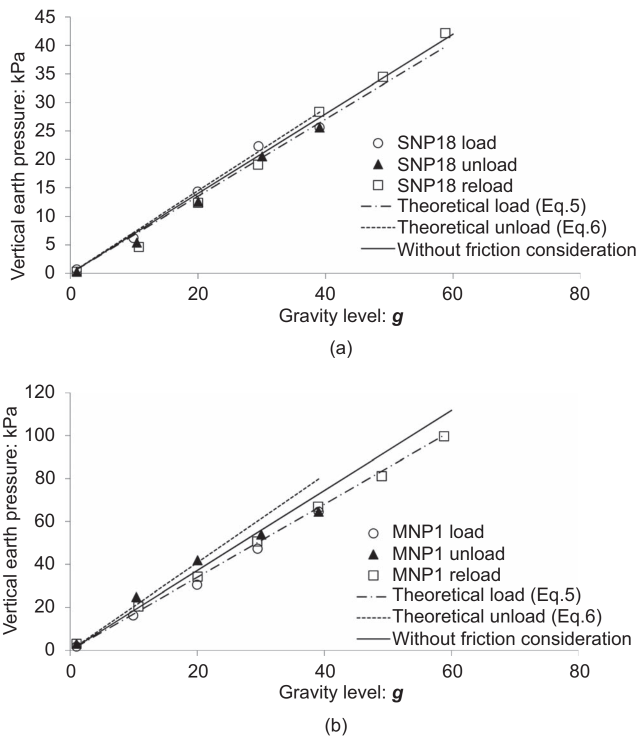

Figure 6. Friction consideration for vertical stresses: (a) vertical stress in the shallow soil (y_0/b=0·28); (b) vertical stress in the deep soil (y_0/b=0·74)

shows theoretical estimations of vertical earth pressure with and without side friction consideration. It can be seen that there is a better fit if friction is considered. This μ should correspond to the average friction ratio of sand–aluminium and sand–PMMA in the centrifuge tests.

3.2 Horizontal earth pressures

Horizontal earth pressure was measured by three pressure cells on both sides of the wall. Figure 7(a) and Figure 7(b) show soil horizontal pressure from SNP14 and SNP15, both mounted in the retaining wall at different depths. Horizontal pressures are found to be higher in unloading than in the loading and reloading stages, showing greater hysteresis than the vertical stress measurements. This is taken to mean that horizontal soil pressures were also influenced by stress history due to the inelastic soil response.

The corresponding theoretical horizontal earth pressures in the loading and reloading stages are drawn on the graph for reference according to

7. $$\sigma_h' = K_0 \sigma_v'$$

where vertical effective stress σ_v' is calculated according to Equation 5, and earth pressure ratio at rest is calculated assuming $K_0 = 1 - \sin\varphi_{crit}'$ as recommended by BS 8002:1994 (BSI, 2001).

Similarly, in the unloading stage, the theoretical horizontal earth pressure is plotted from the following equation

8. $$\sigma_h' = K_{0,OCR} \sigma_v'$$

where σ_v' is calculated according to Equation 6, and $K_{0,OCR}$ is the earth pressure ratio at rest in over-consolidation. According to Mayne and Kulhawy (1982), the horizontal earth pressure ratio in over-consolidated soil would fit

9. $$K_{0,OCR} = \min\left[(1-\sin\phi')\mathrm{OCR}^{\sin\phi'}, K_p\right]$$

where OCR is overconsolidation ratio and ϕ' is the sand friction angle, which is assumed here to be ϕ_{crit}'. The full passive earth pressure coefficient K_p is used here as an upper bound for earth pressure ratio at rest.

In Figure 7(a), Equation 7 predicts the earth pressure reasonably well, although the horizontal stress falls 25% below the

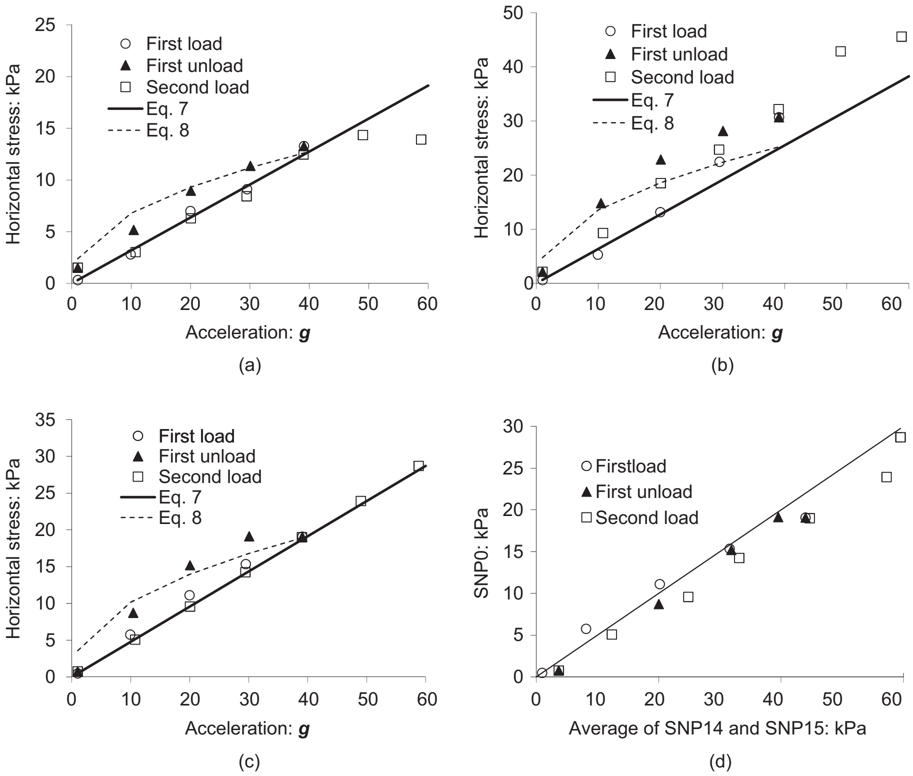

Figure 7. Horizontal earth pressure measurements in spin-up stage: (a) SNP14, shallow depth on the passive side; (b) SNP15, deep on the passive side; (c) SNP0, on the active side; (d) comparisons

theoretical estimation at 60g. In Figure 7(b), both Equation 7 and Equation 8 fall below the pressure measurements due to the additional down-drag from the wall.

Figure 7(c) shows earth pressure measurements from SNP0, which was buried in the soil to measure horizontal soil stress on the retained side. Again measurements during loading and reloading matched well, and hysteresis can be observed in the unloading stage. The earth pressure closely fitted the theoretical estimation of Equation 7 and Equation 8.

As the depth of pressure cell SNP0 was the average of the depths of SNP14 and SNP15, the two pressure cells fixed in the wall on the passive side, it was expected that SNP0 measurements should be the average of SNP14 and SNP15. This is verified in Figure 7(d), in which most data points are around the 1:1 line.

In engineering practice, the effective horizontal earth pressure in sand is usually assumed to be proportional to the vertical effective stress at the same depth, as indicated in Equation 3. With horizontal earth pressure measurements in the loading and reloading stages, this linearity is checked by plotting horizontal pressure against vertical earth pressure at the same depth (Equation 6), as shown in Figure 8. Earth pressures from loading and reloading stages in SNP0 and SNP14 are included in the figure. The gradient of the best fit straight line is found to be 0·474, close to the textbook estimation of the earth pressure coefficient at rest ($K_0 = 1 - \sin\phi'_{\text{crit}} = 0.46$).

4. Experimental observations during excavation

Excavation was carried out by the in-flight scraper after the spin up stage. At each step, 3 mm of sand was removed on the excavated side. Retaining wall failure was not observed even when all the sand (125 mm) on the passive side had been removed. The excavation continued to 135 mm depth, when significant rotation around the top prop was observed. Earth pressures during the excavation were measured by the soil pressure cells.

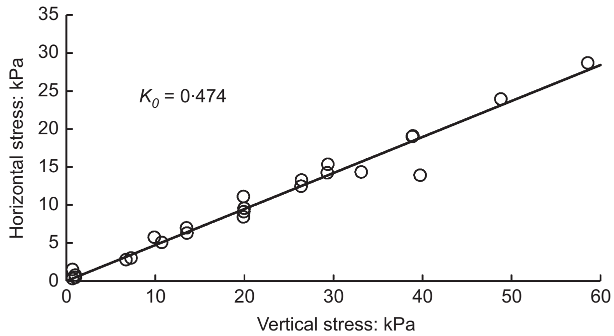

Figure 8. Horizontal earth pressures in loading and reloading for SNP0 and SNP14

4.1 Scraper penetration effect

Compared to earlier excavation techniques such as the heavy fluid method and the stop–start method, in-flight scraping is apparently able to simulate excavations more realistically. During in-flight scraping, each time the scraper (Figure 9) removes a layer of sand, it has to be driven 3 mm into the sand before dragging sand away towards the slope and the bin. It became apparent, however, that the scraper penetration induced an additional stress distribution beneath the scraper. In excavation practice, this situation must also arise when a heavy excavator works close to a retaining wall. The influence of this scraper effect is analysed here.

Figure 10 shows the development of horizontal stress measured at pressure cell SNP14, which was installed in the wall facing the excavated side. When excavation proceeds, the horizontal earth pressure beneath the blade firstly increases and then reduces. The jump of horizontal earth pressure due to scraper penetration could be sensed by the pressure cell each time the scraper was inserted above it (from 10^4 s). The maximum stress jump appeared when the scraper was at about the same level as the top of the pressure cell.

For each cycle of sand scraping, scraper penetration compacts the sand beneath the scraper blade and increases the soil pressure. When the scraper is removed laterally, the soil pressure does not go back to its original value. Bolton (1991) studied stress under a compaction roller on fully drained

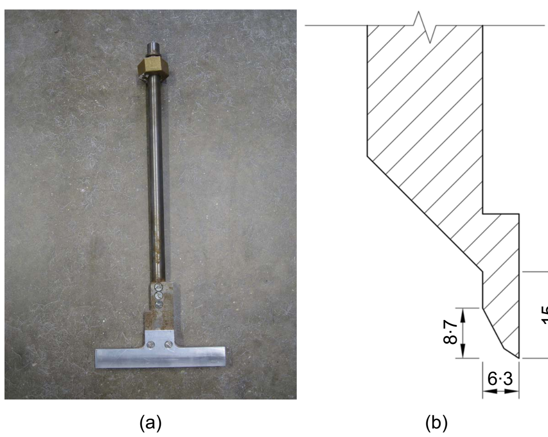

Figure 9. Sand scraper for in-flight excavation: (a) overview of T-shape scraper; (b) dimensions of the scraper's head (in mm)

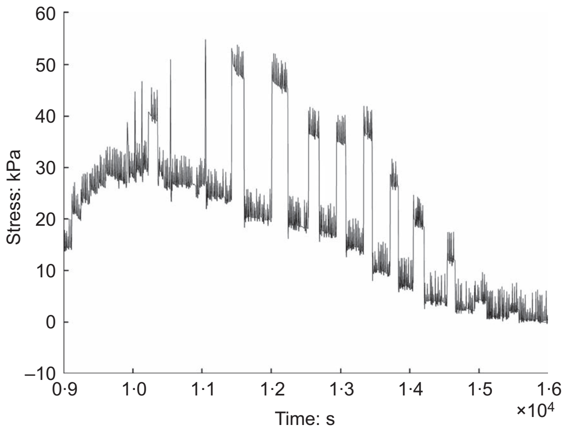

Figure 10. Horizontal stress on the excavated side of the wall during excavation

granular material using the equilibrium method and plasticity. The scraper penetration during in-flight excavation is similar to a single round of soil compaction. The equivalent compaction pressure can be estimated according to the shallow foundation bearing capacity equation (Powrie, 2004)

$$\frac{v_{\mathrm{ult}}}{B} = \sigma_{\mathrm{ult}} = s_{\mathrm{q}} N_{\mathrm{q}} \sigma'_{\mathrm{v},0} + s_{\gamma} N_{\gamma} \frac{\gamma_{\mathrm{soil}} B}{2} \quad (10)$$

The bearing capacity factors N_{q} and N_{γ} account for surcharge and self-weight of the foundation soil respectively, and s_{q} and s_{γ} are shape correction factors. $\sigma'_{\mathrm{v},0}$ is the effective vertical stress at the level of foundation base. During the test, the scraper blade penetrates 3 mm below the original sand surface adjacent to the wall, and accordingly causes additional heave which is thought to bring the blade into contact with the sand across its whole 6·3 mm width (see Figure 9(b)). Such change-of-geometry effects are inherent in modelling construction processes, but are difficult analytically. Nevertheless, the inserted blade is approximated here as a shallow foundation with width B=6·3 mm with a surcharge of 3 mm thickness of sand, having mobilised its full bearing capacity. By applying Prandtl's extended equation as recommended in Eurocode 7 (BSI, 2007), and taking ϕ' to be the critical state angle (33°), we obtain bearing capacity factors N_{q}=26, N_{γ}=33. Thus the equivalent compaction stress $\sigma_{\mathrm{ult}}=V_{\mathrm{ult}}/B$=152 kPa, and the compaction force per unit width $V_{\mathrm{ult}}=\sigma_{\mathrm{ult}}B$=958 N/m.

According to Bolton (1991), when the scraper penetrates, the plastic stress distribution underneath the inserted scraper can be generalised by the following equations.

Vertical stress increase due to compaction

$$\begin{aligned} \Delta\sigma'_{\mathrm{v}} &= \sigma_{\mathrm{ult}} \quad \text{for} \quad z \leq B \\ \Delta\sigma'_{\mathrm{v}} &= \sigma_{\mathrm{ult}} \frac{B}{z} \quad \text{for} \quad z > B \end{aligned} \quad (11)$$

Horizontal stress increase

$$\begin{aligned} \Delta\sigma'_{\mathrm{h}} &= K_{\mathrm{a}} \sigma_{\mathrm{ult}} \quad \text{for} \quad z \leq B \\ \Delta\sigma'_{\mathrm{h}} &= K_{\mathrm{a}} \sigma_{\mathrm{ult}} \frac{B}{z} \quad \text{for} \quad z > B \end{aligned} \quad (12)$$

In the equations above, z is the distance between the point calculated and the bottom of the blade, $\Delta\sigma'_{\mathrm{v}}$ is the vertical stress increment, $\Delta\sigma'_{\mathrm{h}}$ is the horizontal stress increment and K_{a} is fully active earth pressure coefficient. This theory is compared with pressure cell measurements in Figure 11. The residual stress is ignored here as it is much smaller than the stress when the blade penetrates. Note that the pressure cell only registers a full face of sand when the distance under the excavated soil surface exceeds 11·5 mm. When the distance is smaller than 11·5 mm, the actual earth pressure must be larger than the pressure cell measurements. When the distance is larger than 11·5 mm, the pressure cell measurements fit the prediction reasonably well.

When the scraper is removed from the side of the wall, a certain soil pressure will be 'locked-in' in the excavated area. According to the simplification introduced by Broms (1971) and used in Ingold (1979) in the first rational assessment of post-compaction stresses, horizontal compaction stress will be locked-in unless it reaches its passive limit, shown as BC in the simplified load–unload path ABCD in Figure 12(a). In the analysis conducted by Bolton (1991), however, K_0 is taken to vary with overconsolidation ratio during one-dimensional unloading, increasing from K_{a} towards K_{p}. The horizontal stress at depth z after unloading can then be expressed by the following equations

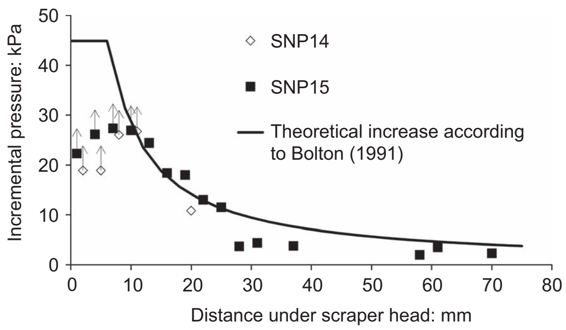

Figure 11. Horizontal earth pressure increment due to scraper penetration

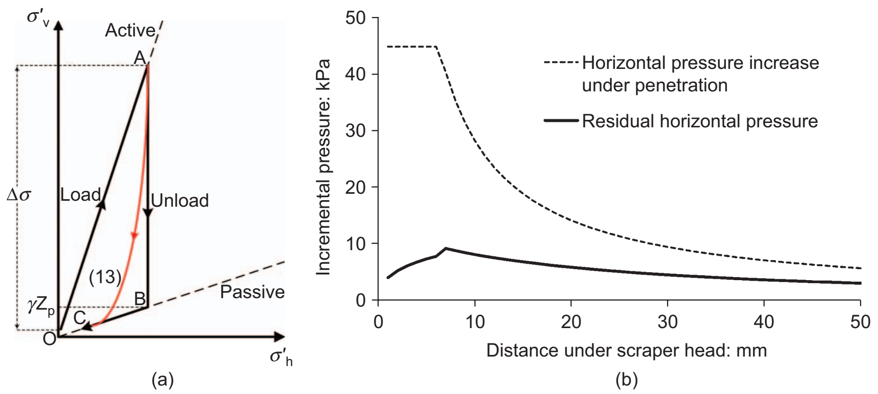

Figure 12. Soil stress changes during and after scraper penetration: (a) compaction stress-path; (b) horizontal pressure increase due to scraper

$$\sigma_h' = K_a \gamma_{soil} z \left[1 + \sqrt{\frac{N_\gamma}{2}} \sqrt{\frac{Q}{\gamma_{soil} z^2}} \right]^{\phi'} \quad \text{for} \quad z \leq B$$

13.

$$\sigma_h' = K_a \gamma_{soil} z \left[1 + \frac{Q}{\gamma_{soil} z^2} \right]^{\phi'} \quad \text{for} \quad z > B$$

The corresponding, and more realistic, unloading path is also sketched in Figure 12(a). Therefore the increase of horizontal pressure after the scraper moves away can also be estimated (see Figure 12(b)). The maximum residual horizontal stress due to scraper penetration is about 9·2 kPa.

4.2 Vertical and horizontal earth pressures during excavation

The vertical earth pressure measurements on the retained side of the wall during excavation are shown in Figure 13. The theoretical vertical pressures according to Equation 2 are plotted together for reference. The solid line is the theoretical vertical pressure shared by MNP0 and MNP1, as they were buried in the same depth. The dash-dot line is the theoretical value for SNP18. Negligible changes of vertical stress occur until the excavation depth exceeds 130 mm. The readings in MNP0 were above the theoretical line, due to the down-drag of the wall. The readings in MNP1 were below the theoretical line, because of boundary friction. For SNP18, the theoretical pressure fits the measured values within an average error of 5%, as friction does not influence the results as much. When the excavation reaches 130 mm, the vertical pressure at MNP0 (around the wall toe) decreases significantly. Earth pressure at SNP18 also decreased but more gently.

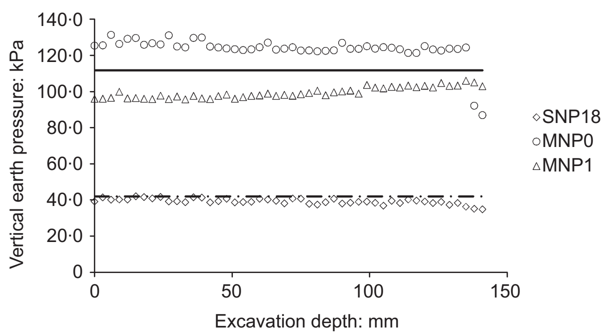

Figure 13. Vertical earth pressure during excavation

Figure 14(a) presents horizontal earth pressure measurements on the active side during excavation. A K_0 line is drawn assuming $K_0 = 1 - \sin\phi'$, while ϕ is taken as ϕ'_{crit}. A K_a line is drawn for reference according to

14. $$K_a = \frac{1 - \sin\phi'}{1 + \sin\phi'}$$

Here ϕ' is taken as peak friction angle ϕ'_{max}. The pressure cell is embedded at 75 mm depth. The mean effective stress p' is 40 kPa if the horizontal stresses are assumed to be in a K_0 condition. As the relative density of the soil is 47%, and according to Bolton (1986), ϕ'_{max} is 43° in plane strain conditions.

As shown in the figure, at small excavation depths (0–30 mm) when the soil movements are negligibly small, the horizontal earth pressure coefficient is close to K_0. When the excavation depth is larger, the horizontal pressure starts to drop. When excavation proceeds to 75 mm, and while the maximum soil movements were still smaller than 0·1 mm, the horizontal pressure starts to drop. When the excavation depth exceeds

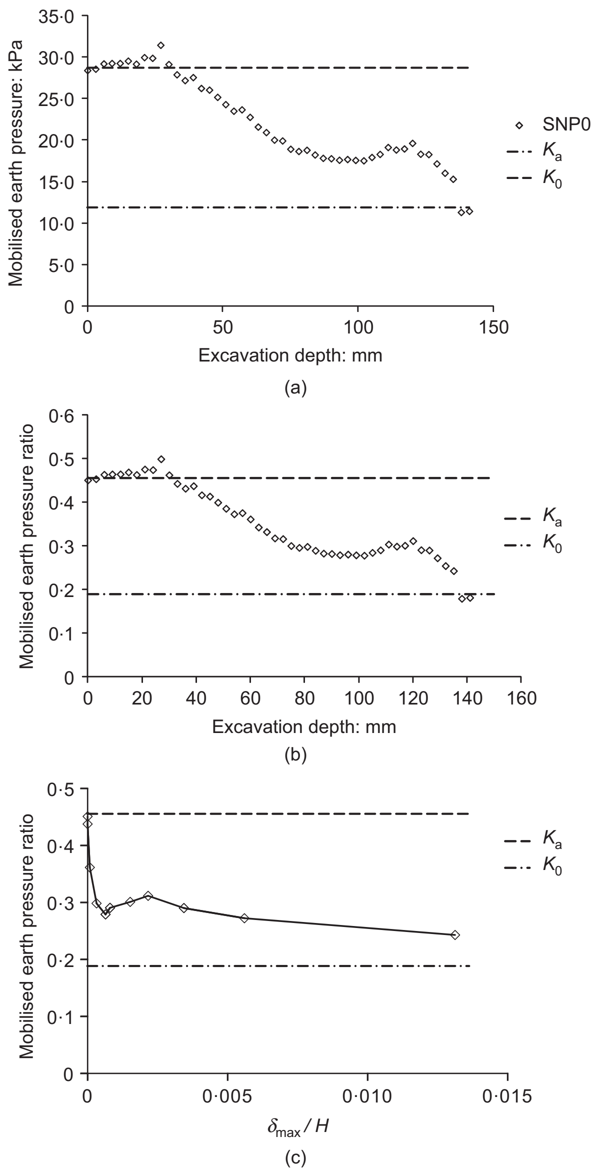

Figure 14. Horizontal earth pressure on the retained side of the wall: (a) mobilised earth pressure against excavation depth; (b) mobilised earth pressure ratio against excavation depth; (c) mobilised earth pressure ratio against soil movement

125 mm (full wall length), the horizontal pressure drops to the K_a line.

If the horizontal earth pressure ratio K is defined as

$$15. \quad K = \frac{\sigma_h'}{\sigma_v'}$$

its value on the retained side of the wall can be plotted as shown in Figure 14(b). As the vertical earth pressure was constant during excavation, the change of the earth pressure coefficient was similar to Figure 14(a). If the ratio of maximum horizontal wall movement δ_{max} and total wall length H is taken as an indicator of soil movement, the active earth pressure ratio at each dimensionless δ_{max}/H value is shown in Figure 14(c). It is shown that the earth pressure ratio decreased very sharply for a small wall deflection ($\delta_{max}/H=0{\cdot}001$), which is consistent with Terzaghi's finding about the relationship between earth pressure coefficient and wall rotation angle (plotted by Clayton and Milititsky, 1986). A much milder decrease at large wall deflections is also observed until the end of the test ($\delta_{max}/H=0{\cdot}012$).

Figure 15(a) shows horizontal earth pressure observed from pressure cell SNP14 on the passive side. The maximum passive pressure line (K_p line) is drawn for reference according to the distance between the soil surface and the cell centre, and the maximum passive earth pressure coefficient

$$16. \quad K_p = \frac{1+\sin\phi'}{1-\sin\phi'}$$

Here ϕ' is also taken as $\phi'_{max}=43^o$. Similarly a K_0 line is drawn according to Equation 3. In theory, the horizontal pressure on the passive side should always be between the K_0 line and the K_p line. As the depth of sand over the two cells reduces when sand is being removed, both the K_0 line and the K_p line have a negative gradient, intersecting on the horizontal axis at the embedment depths of the cell centres.

The pressure cell registered K_0 earth pressures before excavation started. At a small excavation depth (0–30 mm), when the horizontal earth pressure on the active side was almost constant, the horizontal earth pressure on the passive side increased to maintain global equilibrium of the retaining wall. When excavation had proceeded to within 30 mm of the cell centres, however, the registered earth pressures began to decrease. This is taken as a sign of the non-linearity of the mobilised earth pressure distribution on the passive side. Most of the earth pressure measurements nevertheless stayed within the bounds of the K_0 and K_p lines. However, some data exceeded the K_p line as the dredge level approached closer to the centre of the pressure cells. Furthermore, the pressure cell continued to register some pressure when the excavation depth exceeded that of the cell centre. These abnormalities are due to the size of the pressure cells. The diameter of the sensing face of the pressure cells was 23 mm. When the excavation dropped to within 11·5 mm of the cell centre only part of the cell was buried in sand, and the sensing diaphragm accordingly under-registered the actual lateral earth pressure. Similarly, some earth pressure continued to be registered until the excavation had proceeded 11·5 mm beyond the cell centre.

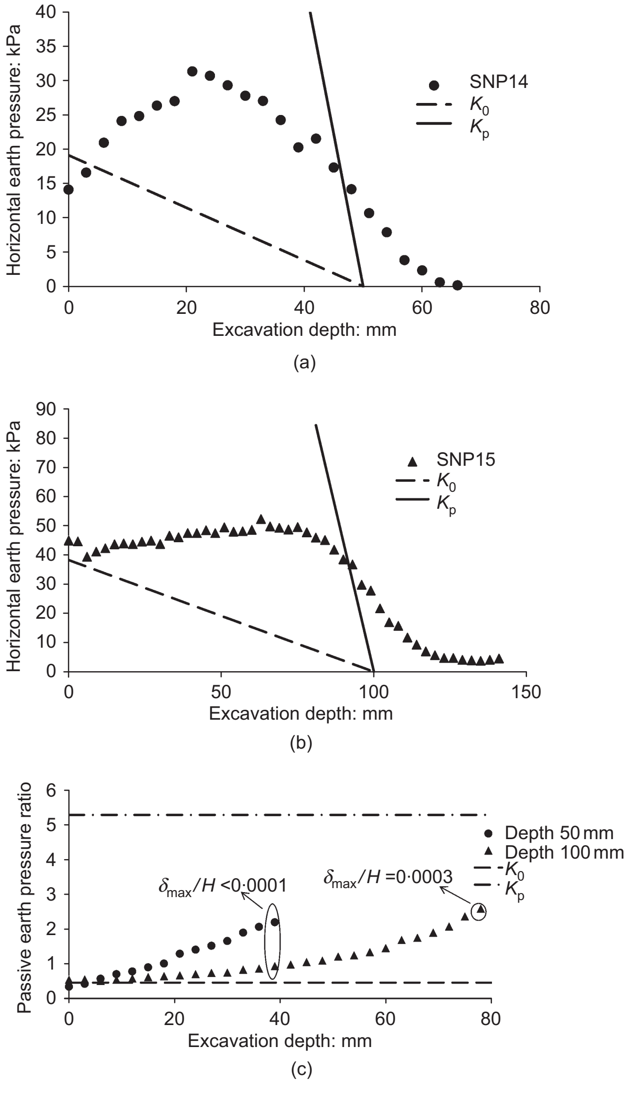

Figure 15. Horizontal earth pressure on the passive side: (a) horizontal earth pressure on the shallow pressure cell; (b) horizontal earth pressure on the deep pressure cell; (c) passive earth pressure ratio during excavation

Figure 15(b) shows the horizontal earth pressure from a deeper cell SNP15. If the inaccurate measurement when excavation depth exceeds 88·5 mm is ignored, the passive earth pressure mobilised at 100 mm depth kept increasing beneath the excavation. The lateral earth pressure at SNP15 moved from the K_0 line to the K_p line at 80 mm excavation depth.

The passive earth pressure ratios at the centres of the two pressure cells (50 mm depth and 100 mm depth) are shown separately in Figure 15(c). As excavation proceeded, the passive earth pressure ratios at both depths increased throughout the excavation from K_0 to an ultimate value of about 2·5. This is much smaller than fully mobilised passive pressure ratio K_p calculated from ϕ'_{max} because failure happens later when both pressure cells had been exposed. Although information is distorted or missing when the excavation level approaches and passes the cell centre, the plot shows that passive earth pressure does not fully mobilise proportionally throughout the excavated region. For a certain excavation depth, the passive earth pressure ratios are not the same at different depths, showing that passive earth pressure is not distributed linearly. The observation of a non-linear distribution of passive earth pressure below the current excavation level, during construction, shows the inaccuracy of simulating excavation by the draining of a heavy fluid.

5. Conclusions

A centrifuge model test is presented simulating a top-propped excavation in medium-loose sand. A new earth pressure measurement technique, the null soil pressure gauge, was used in a centrifuge model for the first time and reliable results were obtained.

Less than 10% reduction in vertical stress due to boundary friction was observed at a proportional depth $y_0/b=0{\cdot}74$. Boundary friction also causes vertical stress increases in sand following unloading, and the hysteresis in measured vertical stresses accompanying g-level cycles offers the centrifuge modeller a convenient way of inferring friction effects. The average friction coefficient between the soil and the inside surfaces of the centrifuge strong box was estimated to be $\mu=0{\cdot}27$ through the application of a simple silo model.

Prior to excavation, the conventional calculation of earth pressures 'at rest' with $K_0=1-\sin\phi_{crit}$ was shown to be in good accord with the measurements. During the excavation, the evolution of the horizontal pressure ratios was monitored. Contrary to the common assumption, the earth pressure ratio on the passive side of the wall is not constant during excavation. This militates against the use of the heavy-fluid technique to simulate excavation in a centrifuge test.

The use of more realistic excavation technology, in this case a full-width scraper blade, brings an additional element into the situation, however; insertion of the blade causes a pressure spike in the sand below which enhances earth pressures on the excavated side of the wall. A method of estimating its magnitude was demonstrated.

Postscript

Tragically, Dr Yuchen Li went missing on Malaysia Airlines flight MH370 on Saturday 8 March 2014, just two days after this paper was accepted for publication. He was returning to the Beijing office of Schlumberger after attending a training course in Kuala Lumpur.

Acknowledgements

The work was supported by Cambridge Overseas Trust and the China Scholarship Council.

REFERENCES

Bolton MD (1986) The strength and dilatancy of sands. *Géotechnique* **36(1)**: 65–78.

Bolton MD (1991) *Geotechnical stress analysis for bridge abutment design*. Transport and Road Research Laboratory, Crowthorne, UK, TRRL contractor report 270.

Broms BB (1971) Lateral pressures due to compaction of cohesionless soils. In *Proceedings of the 4th Conference on Soil Mechanics, Stockholm, Sweden*, pp. 373–384.

BSI (2001) *BS 8002. Code of Practice for Earth Retaining Structures*. BSI, London, UK.

BSI (2007) *BS EN 1997-1:2004. Eurocode 7. Geotechnical Design. General Rules*. BSI, London, UK.

Clayton CRI and Bica AVD (1993) The design of diaphragm-type boundary total stress cells. *Géotechnique* **43(4)**: 523–535.

Clayton CRI and Milititsky J (1986) *Earth Pressure and Earth-Retaining Structures*. Surrey University Press, Glasgow and London, UK, p. 16.

Dave T and Dasaka SM (2011) A review on earth pressure measurement using earth pressure cell. *International Journal of Earth Sciences and Engineering* **4(6 SPL)**: 1031–1034.

Haigh SK, Houghton NE, Lam SY, Li Z and Wallbridge PJ (2010) Development of a 2D servo-actuator for novel centrifuge modelling. In *Proceedings of the 7th International Conference of Physical Modelling in Geotechnics, Zurich, Switzerland*, pp. 239–244.

Ingold TS (1979) The effects of compaction on retaining walls. *Geotechnique* **29(3)**: 265–283.

Li Y (2013) *Ground Movements Due to Excavation in Cohesionless Soil: Physical and Analytical Models*. PhD thesis, University of Cambridge, Cambridge, UK.

Madabhushi SPG, Houghton NE and Haigh SK (2006) A new automatic sand pourer for model preparation at University of Cambridge. In *Proceedings of the 6th International Conference of Physical Modelling in Geotechnics, Hong Kong*, pp. 217–222.

Mayne PW and Kulhawy FH (1982) K0-OCR relationships in soil. *Journal of the Geotechnical Engineering Division* **108(6)**: 851–872.

Powrie W (2004) *Soil Mechanics: Concepts and Applications*, 2nd edn. Spon Press, Oxford, UK.

Santamarina JC and Goodings DJ (1989) Centrifuge modeling: a study of similarity. *Geotechnical Testing Journal* **12(2)**: 163–166.

Stringer ME (2012) *The Axial Behaviour of Piled Foundations in Liquefiable Soil*. PhD thesis, University of Cambridge, Canbridge, UK.

Take WA and Valsangkar AJ (2001) Earth pressures on unyielding retaining walls of narrow backfill width. *Canadian Geotechnical Journal* **38(6)**: 1220–1230.

Talesnick ML (2005) Measuring soil contact pressure on a solid boundary and quantifying soil arching. *Geotechnical Testing Journal* **28(2)**: 1–9.

Talesnick ML (2013) Measuring soil pressure within a soil mass. *Canadian Geotechnical Journal* **50(7)**: 716–722.

Talesnick ML, Horany H, Dancygier AN and Karinski YS (2008) Measuring soil pressure on a buried model structure for the validation of quantitative frameworks. *Journal of Geotechnical and Geoenvironmental Engineering* **134(6)**: 855–865.

Talesnick ML, Xia HW and Moore ID (2011) Earth pressure measurements on buried HDPE pipe. *Géotechnique* **61(9)**: 721–732.

Talesnick ML, Ringel M and Avraham R (2014) Measurement of contact soil pressure in physical modelling of soil–structure interaction. *International Journal of Physical Modelling in Geotechnics* **14(1)**: 3–12, http://dx.doi.org/10.1680/ijpmg.13.00008.

White DJ, Take WA and Bolton MD (2003) Soil deformation measurement using particle image velocimetry (PIV) and photogrammetry. *Géotechnique* **53(7)**: 619–631.